metals

MDPI

Article

Modeling Friction Stir Welding: On Prediction and Numerical Tool Development

Max Hossfeld †

Innovation Campus Future Mobility, University of Stuttgart, Nobelstraße 15, 70569 Stuttgart, Germany; max.hossfeld@ifsw.uni-stuttgart.de

† Former affiliation: Materials Testing Institute, University of Stuttgart, 70569 Stuttgart, Germany.

Abstract: This paper reports on a simulation framework capable of predicting the outcomes of the friction stir welding process. Numerical tool development becomes directly possible without the need for previous calibration to welding experiments. The predictive power of the framework is demonstrated by a case study for numerical tool development and validated experimentally. Different tool geometries with high levels of detail and active material flow features are investigated, and their effect on the process outcomes is quantified. The simulation framework is found to be able to predict forces, material flow, temperature fields, weld formation and welding defects a priori, in detail and precisely. This applies to the outer appearance of the weld as well as the location, shape, and size of inner welding defects. Causes for defects can be identified, analyzed and remedied. Compared to the validation experiment, the simulation showed a slight overestimation of the process impact in the case study. Since the framework relies strictly on analytically describable physics, the efforts for modeling the process are moderate considering the precision of the results.

Keywords: friction stir welding; simulation; tool development; tool design; CEL; ALE; numerical modeling; prediction

Citation: Hossfeld, M. Modeling Friction Stir Welding: On Prediction and Numerical Tool Development. *Metals* **2022**, *12*, 1432. https://doi.org/10.3390/met12091432

Academic Editors: Koh-ichi Sugimoto and Michael Regev

Received: 22 July 2022
Accepted: 25 August 2022
Published: 29 August 2022

1. Introduction

Since the whole friction stir welding (FSW) process [1] is established by the contact of tool and workpiece only, tool geometry and material selection are crucial both for weld quality and economic efficiency. But today, and so after more than two decades of industrial use and scientific research, tool design and development for FSW are still particularly a matter of implicit expert knowledge, incremental design changes, and trial and error [2,3]. This issue mainly arises from the difficulty to observe the actual joining process within the joining zone directly, e.g., since it has to be steadily covered to ensure FSW's mechanical working principle [4,5]. Moreover, the FSW process itself compromises several highly coupled (non-linear) phenomena and their manifold interactions, such as frictional and plastic heat generation, material flow and large plastic material deformation, tool/workpiece interaction or temperature-dependent material behavior [5–8]. Despite extensive research activities and advances regarding all of FSW's process phenomena in recent decades, those and especially their interactions are still not fully understood [5,9–12]. This leads directly to several issues regarding tool development and design: while the effects of smaller, incremental geometrical changes may yet be anticipated by experts in spite of their non-linear nature, the complexity of interacting process phenomena makes it almost impossible to predict the effects of more extensive, detailed, or also uncommon geometrical changes or new designs, cmp [13–15]. This applies in particular when more than one geometrical feature is changed at once, process parameters are simultaneously adjusted, or effects such as tool wear should be considered. As a consequence, tooling concepts in FSW have evolved comparatively slowly during the last decades and are today mostly based on experimentally proven tool designs. Many of the respective geometrical features can be found already

in very early studies in the 1990s, such as in TWI's GSP 5651 [16]. Those are, for example, using flats, threads and flutes on the pin [17] or concentric grooves or scrolls as shoulder profile [18]. So today, tooling concepts in FSW show a very high degree of self-similarity, while at the same time, neither have standard FSW tool designs ever been incorporated into standards or specifications such as ISO 25239-1:2020 or AWS D17.3/D17.3M:2016 [19], nor does a commonly accepted standard procedure for tool development in FSW exist.

A possibility to gain access to FSW's adversely observable process phenomena is numerical modeling. Especially during the last decade, several thermo-mechanically coupled 3D simulation models have been proposed, which have contributed extensively to the process understanding of FSW. Guerdoux and Fourment modeled FSW in Forge3D® using an arbitrary Lagrangian–Eulerian (ALE) formulation and showed that it is possible to predict process forces after a calibration of the contact conditions between plate and a simplified tool geometry [20]. Assidi et al. extended this consideration by adapting more extensive friction models to their data and showed that the calculation of process temperatures inside the joining zone is possible [21]. Own work using the coupled Eulerian-Lagrangian (CEL) formulation of Abaqus/Explicit showed that simulating the whole FSW process with real tool geometries and the joining of two separate sheets into one within one continuous model is feasible, while forces, micro-structure, welding defects, and their evolution such as voids/wormholes and burring can be represented [5,22]. Both approaches, ALE and CEL, are comparatively computationally intensive and, depending on the level of detail, require up to several days of computing time to simulate some seconds of the FSW process, cmp [5,23]. Research carried out using Smoothed-Particle Hydrodynamics (SPH) and graphics processing units (GPUs) improved this issue significantly, but partly at the expense of the level of detail. Fraser et al. showed that by using a simulation code called SPHriction-3D, void and burr formation in FSW can be represented and provided an artificial process window based on a virtual parameter study [24]. Bagheri et al. used SPH to investigate the temperature history, strain and stress distributions during conventional as well as submerged FSW (SFSW) [25]. Simplified tool geometries were used in both studies. Apart from thermo-mechanically coupled simulation models, pure CFD approaches have been shown to be suitable for investigating real FSW tool geometries as well. These investigations usually focus on the analysis of the steady state of the process during traversing [26–28] since it is barely possible to represent the whole process sequence, i.e., plunging/dwelling, traversing and exiting, in one continuous simulation model due to methodical limitations. This is in particular relevant because the process history, i.e., how the steady state was reached, may affect the steady state of the FSW process.

Numerical modeling may be well suited and a great opportunity for investigating tool geometries without the need of manufacturing those. Tool designs could be assessed and the FSW process optimized virtually saving resources such as time and money while providing new insights. However, no consistent simulation framework or methodology for numerical tool development or process prediction has been proposed, nor has its principal feasibility been shown to date. Numerical models are still calibrated iteratively on experiments, which considerably reduces the predictive power for extrapolations [7]. Therefore, this study proposes a simulation framework capable of predicting the outcomes of the FSW process. By this, it can directly be used for virtual tool development. The predictive power is assessed by a numerical tool development case study.

2. Materials and Methods

The procedure of this study is as follows: In a first step, a base tool geometry and a fixed parameter set, which is known to cause a welding defect are defined. Complementarily, a material flow feature is defined for the pin which can potentially solve this issue. Starting with the base geometry, simulations are then carried out, and the resulting size of the welding defect is analyzed. As long as a welding defect is found, the geometrical feature on the pin is subsequently enlarged, and the simulation is repeated with the new tool geometry. This procedure is continued until either no welding defect is detected in the

simulation anymore or the tool geometry cannot be adjusted any further. For ensuring that the study is not influenced, e.g., by calibration or confirmation bias, the simulations of all tool geometries are carried out before any real welding trials are performed.

2.1. Tool Geometries, Material Flow Feature, Process Parameters

The base geometry shown in Figure 1 was chosen on practical experience. Simple rotationally symmetrical designs without any active material flow structures, such as the truncated cone chosen for this study, usually lead to a stable weld defect formation at welding depths above three millimeters and common industrial welding speeds [29]. The reason for this is mainly an insufficient heat transport to the bottom of the pin and also a lower level of heat input of the pin itself, causing a "lack of consolidation" [30] and thus void defects.

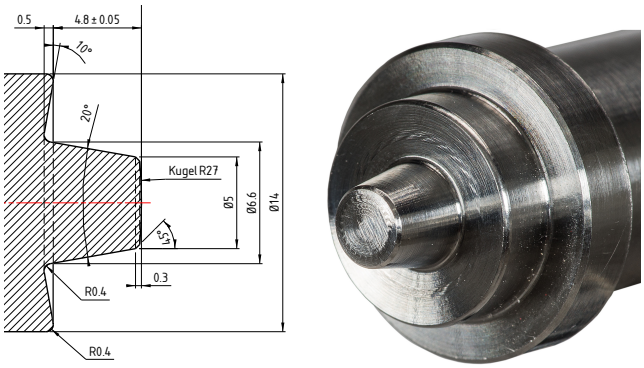

Figure 1. Base geometry: relevant dimensions and manufactured tool made from QRO® 90.

Consequently, three spiral grooves also known as flutes were chosen as complementary material flow feature. This feature is well proven for preventing void defects in FSW by transporting heat from the shoulder to the bottom of the pin, homogenizing the weld's temperature profile, improving the material flow, and additionally compressing the stirred material. The three spiral grooves were arranged evenly on the pin, i.e., with 120 degree offset to each other, and had a 45 degree pitch angle (Figure 2). The starting width of the spiral groves was set to 1 mm. After that, all further enlargements of the grooves were made in steps of 0.4 mm, i.e., 1 mm–1.4 mm–1.8 mm and so on. All tools for the later experimental validation of the simulation were made of QRO® 90 hot-working tool steel, hardened and annealed to 45 HRC. The material properties are given in Table 1. For the later manufacturing, the basic geometry was turned first from bar stock, and a reference was machined. Then the respective material flow feature was generated by a ball nose end mill with a 0.5 mm radius. For simplicity, the depth of the respective structure was always chosen as one third of its width.

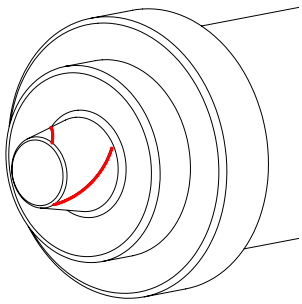

Figure 2. Definition, location and arrangement of the complementary material flow feature (**red**) as a superposition on the base tool geometry.

Table 1. Temperature-dependent material properties of QRO® 90 (hardened and annealed to 45 HRC) derived from manufacturer's information.

Temperature [°C]	**20**	**400**	**600**
density [kg/m³]	7800	7700	7600
thermal conductivity [W/mK]	33	33	33
Young's modulus [GPa]	210	180	140
yield stress [MPa]	1270	1000	620
ultimate tensile stress [MPa]	1470	1200	840

2.2. Joint Geometry and Aluminum Alloy, Welding Setup and Process Parameters

All welds in this study were 5 mm butt welds, all sheets were 300 mm long and 100 mm wide, two each making a joint set-up. As material, AA 6061 in T6 temper was used. The temperature-dependent material properties of AA 6061-T6 were already determined for a previous study [29] and are summarized in Figure 3. The same process parameter set was used for all welding experiments. It was derived from a related industrial application. The parameters were a spindle speed of $n = 1400\,\mathrm{min}^{-1}$, a traverse speed of $v_x = 400\,\mathrm{mm/min}$, and a tilt angle of $\alpha = 2°$. Further process parameters include a plunging speed of $v_z = 40\,\mathrm{mm/min}$, a dwelling time of 1 s, and a linear ramp up/ramp down for the first and last 20 mm of the weld. The welding was carried out on a MTI GG-1 gimbaled gantry FSW machine, capable of recording all relevant process variables, such as spindle torque or X, Y and Z-forces with about 100 Hz.

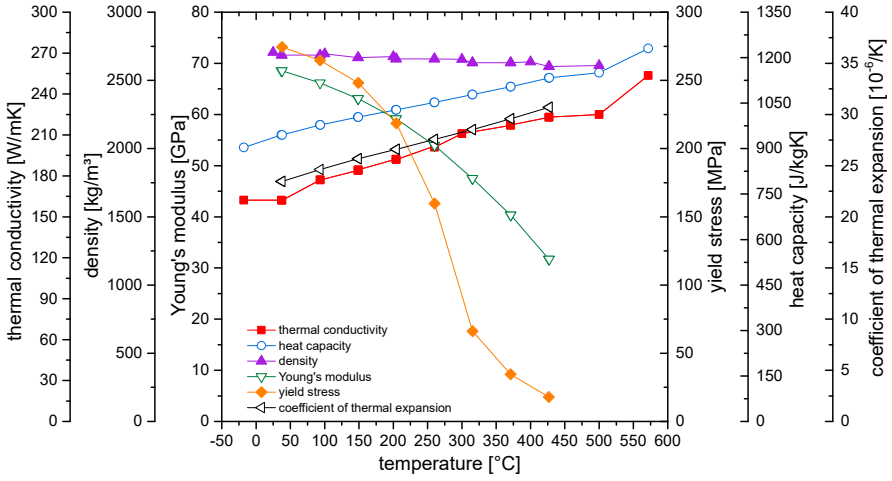

Figure 3. Temperature-dependent thermal and mechanical properties of AA 6061-T6.

2.3. Simulation Model

The most important aspect of process modeling, and especially for tool development, is the prediction of unknown real process conditions and outcomes. To achieve this and to maximize the applicability and general validity, the model design is based on fundamental physics to avoid any fitting to welding experiments. Based on previous work [5,22] and advantages such as the possibility of simulating the whole process within one continuous model and the high detail of representing the surface formation, the CEL formulation of Noh [31] implemented in Abaqus® was used.

2.3.1. Simulation Setup

The essential simulation setup consists of two Eulerian workpieces and a Lagrangian tool. Directly adjacent and thermally and mechanically loaded elements such as backing and fixtures are modeled as Lagrangian bodies as well. Peripherals beyond this, such

as spindle shaft or machine bed, are represented by thermal and mechanical boundary conditions. Independent and overlapping meshes of Eulerian and Lagrangian formulation are used for enabling the interaction between all modeled parts. The Eulerian mesh therefore extends beyond all designated contact regions with the Lagrangian bodies. This allows a free flow of material within the Eulerian mesh and efficiently prevents numerical diffusion at the same time. Figure 4 shows the model setup schematically.

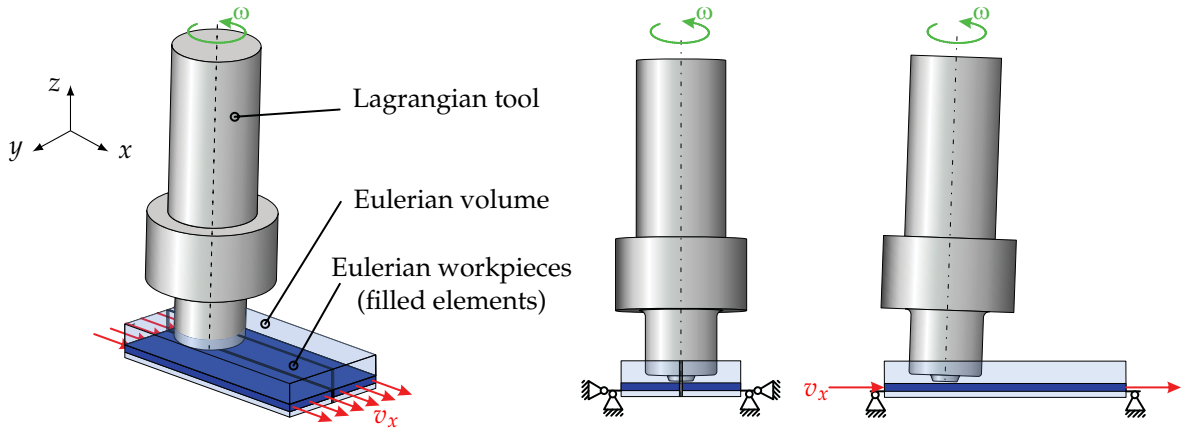

Figure 4. Schematic setup of the numerical model (starting position): isometric, front and side view, shown without tool holder, backing and clamping.

2.3.2. Workpieces

The two workpieces lie completely within the Eulerian mesh and are represented by cells partially filled with material (volume of fluid method). With this method, the level of detail regarding the representation of process phenomena and surface reconstruction depends strongly on the mesh fineness. Therefore, the Eulerian mesh consists of 230,000 thermally coupled linear multi-material elements with reduced integration and hourglass control (EC3D8RT). For separating the two workpieces, i.e., representing the joint gap, and for a more robust handling of contact and friction, the mesh in the later contact and joining zone is even finer, as highlighted by the red arrow in Figure 5. To represent the thermal and mechanical material behavior, the data shown in Figure 3 and the Johnson–Cook material model, Equation (1), were applied. The corresponding parameters of the material model for AA 6061-T6 are given in Table 2.

$$\sigma_{\mathrm{y}}(\varepsilon_{\mathrm{v,pl}}, \dot{\varepsilon}_{\mathrm{v,pl}}, T) = \left[A + B(\varepsilon_{\mathrm{v,pl}})^n\right]\left[1 + C\ln(\dot{\varepsilon}^*_{\mathrm{v,pl}})\right][1 - (T^*)^m] \tag{1}$$

$$\text{with} \quad \dot{\varepsilon}^*_{\mathrm{v,pl}} := \frac{\dot{\varepsilon}_{\mathrm{v,pl}}}{\dot{\varepsilon}_{\mathrm{v,pl,0}}} \quad \text{and} \quad T^* := \begin{cases} 0 & \text{for} \quad T < T_0 \\ \dfrac{T - T_0}{T_{\mathrm{S}} - T_0} & \text{for} \quad T_0 \le T \le T_{\mathrm{S}} \\ 1 & \text{for} \quad T > T_{\mathrm{S}} \end{cases} \tag{2}$$

Table 2. Johnson–Cook parameters for AA 6061-T6.

Alloy	A	B	C	n	m
AA 6061 - T6	291	113	0.006	0.42	1.43

2.3.3. Tools

The tool is represented by a linear–elastic Lagrangian body with the material properties of QRO 90 given in Table 1. Between the given support points, a linear interpolation is automatically carried out by the solver. As with the workpieces, a comparatively fine mesh is necessary to map the high level of detail of the tools and to address the representation of complex physical phenomena. Those are especially the contact initiation during plunging

or an actively induced material flow within the tool's structures during traversing. Quite constantly, 700,000 thermally coupled linear elements of type C3D4T were used to mesh each tool design, cmp. Figure 5. Due to their slightly different geometry, number and arrangement of elements vary to some extent between the tool designs.

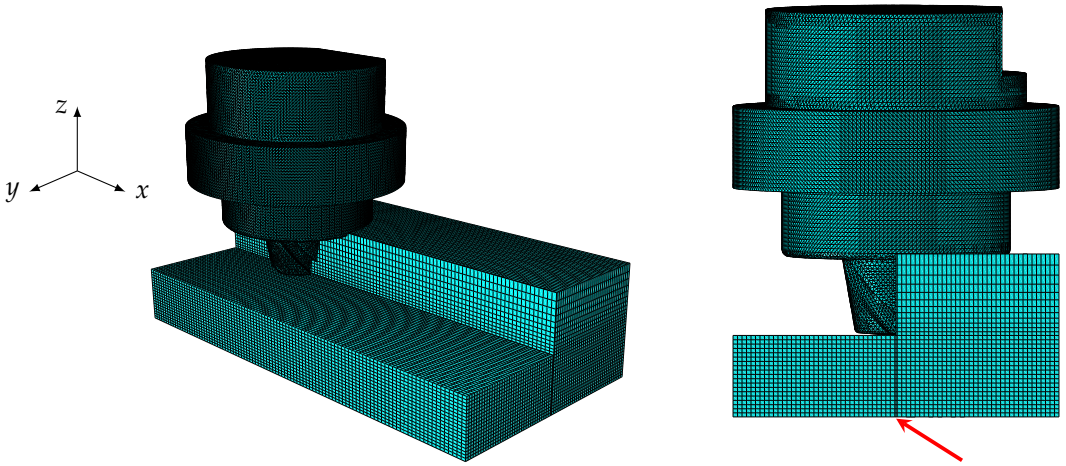

Figure 5. Setup of numerical model with meshing of Lagrangian tool and Eulerian region, isometric and rear view, Eulerian region partially hidden in each case on the left.

2.3.4. Frictional Contact and Formulation, Interactions and Boundary Conditions

For the contact definition in the simulation the *All* with self* contact algorithm of Abaqus was used. By this, the contact between tool and workpieces and its location in the simulation is neither forced nor pre-defined, but takes place automatically when bodies come in contact within the Eulerian volume. Contact conditions are then solved for each node separately. Furthermore, a detachment of the material from the tool during the simulation is possible, which is necessary for the representation of free surfaces or volumetric defects. Moreover, a self-contact of the material is possible as well, which is especially important for the simulation of the joining process of the two workpieces into one, or the simulation of burr formation.

The underlying friction formulation is a visco-plastic approach directly based on the Johnson–Cook material model using the von Mises yield criterion:

$$\tau_{\text{fric}} = \frac{1}{\sqrt{3}}\sigma_{\text{y,J-C}} \tag{3}$$

$$= \frac{1}{\sqrt{3}}\sigma_{\text{y}}(\varepsilon_{\text{v,pl}}, \dot{\varepsilon}_{\text{v,pl}}, T) \tag{4}$$

This formulation results in two significant advantages. First, the direct relation to the material model provides a consistent system, which makes it possible to describe local frictional conditions as a function of temperature, strain rate, stress state, etc., without having to adapt to welding experiments. Second, the description via the material model avoids additional non-linearities and thus contributes considerably to the numerical stability of the simulation since friction phenomena in principle already exhibit a highly nonlinear (parabolic) character.

The heat generated at the friction interface between tool and workpieces is distributed using an approach common in tribology [32–34]. Until a thermal equilibrium is reached, heat is distributed according to the ratio of the (temperature dependent) heat penetration coefficients of the two materials, and after that, according to the ratio of the materials' thermal conductivities, neglecting further thermal damping effects. Figure 6 shows the areas defined for heat conduction and convection on tool and workpieces. Generally, it is defined that all bodies and the environment have a temperature of 20 °C at the beginning

of the simulation. Since a tool holder constantly cooled to 20 °C was used for the welding experiments, a corresponding boundary condition was applied to the shaft of the tool.

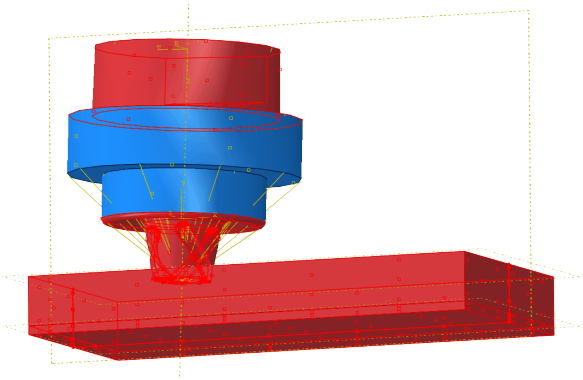

Figure 6. Areas defined for heat conduction (**red**) and convection (**blue**) on tool and workpieces.

2.3.5. Implementation of Process Parameters and Procedure

The process parameters are implemented by a split approach. Spindle speed and movement of the tool in normal or z-direction are implemented with the help of a reference point on the tilted tool's center axis. Moreover, by this reference point, the machine's stiffness in x, y, and z is realized by (linear) spring constraints. At this point, process forces can be read out. The implementation of the tool's traverse speed in x-direction is realized by velocity constraints on the Eulerian volume as already shown in Figure 4. This is done to increase the the numerical stability since the simultaneous linear displacement of a fast rotating tool often leads to numerical instability.

To simulate the process, the tool is set in rotation. Then, the rotating tool is moved along the z-axis until the desired plunging depth in sheets is reached. This position is held until the end of the dwelling step. For traversing, a velocity constraint is then applied on the Eulerian volume by ramping up to the desired traverse speed. After the desired welding is reached, the traverse movement is stopped by ramping down the traverse speed to zero. Subsequently, the tool is extracted from the workpieces.

3. Results

The procedure described in the previous section yielded the following results: The uncontoured base geometry resulted in a continuous formation of a volumetric welding defect in the simulation. The same resulted for the two succeeding tool designs with structure widths of 1.0 and 1.4 mm. The third design iteration with a width of 1.8 mm was then the first to exhibit no wormhole formation in sections during traversing. Very similar results but with a further improving trend were found for the fourth design iteration with 2.2 mm. Finally, for the fifth iteration of the tool design with a structure width of 2.6 mm, no volumetric welding defect could be detected anymore during the simulation.

Based on these results, the third and the fifth design iterations were machined, and welding trials were performed together with the base geometry. An overview of those three tools and their geometrical details is given in Figure 7. Results of the respective simulation and welding trials are presented together and compared in the following subsections.

3.1. Results for Base Geometry

Figure 8 shows the outer appearance of the weld carried out with the base geometry in the simulation and experiment. The weld's outer appearance is comparatively sound and, apart from a small burr formation at the beginning, without any visible welding defects. However, in both cases, a slight elevation of the weld compared to the workpiece surface can be found, which already implies that the material has to be pushed out of the joining zone by the tool. Figure 9 shows a corresponding semi-transparent cut along the welding direction, providing insights to the inner process phenomena. In this view, the

elevation of the weld can be recognized as well and determined to reach up to 0.6 mm ①. This continuous loss of material from the joining zone is directly associated with the formation of an inner cavity (continuity condition). The reason why the weld's outer appearance shows, nonetheless, no visible welding defects can be determined from the cut as well. It is a characteristic defect phenomenon known in FSW [29,30]: The strong and robust material flow regime of the shoulder fully develops initially ③ and remains intact, despite the continuing material loss from the joining zone ④. In the pin flow regime on the advancing side where material flow regimes meet, a stagnation point develops due to the lack of velocity or pressure, respectively. Material flow regimes cannot merge, and a cavity begins forming with the start of the traverse movement behind the tool ②. This cavity evolves into a stable wormhole defect during the steady state of the process, extending 2.2 mm in the thickness direction ⑤. Simultaneously, the material flow at the bottom of the pin remains intact, but separates from other material flow ⑥. Figure 10 shows the barker-etched cross section of the corresponding welding experiment conducted for validation. First, it becomes clear that the location, shape and size of the cavity and also burr formation are predicted with a decent accuracy by the simulation: with an extension of 2.3 mm in thickness direction and covering an area of about 3.4 mm², the wormhole defect reduces the load-bearing cross section of the component by about 46%. With this, the difference in defect size to the numerical result is less than 5% in relative terms. While the horizontal location of simulation and experiment matches the vertical defect location differs. The simulation predicts that the lowest point of the defect will be about 2 mm from the bottom of the sheet. However, from the cross section of the real welding experiment, Figure 10, it is found to be about 1 mm lower, which is 20% of the sheet thickness. As predicted by the simulation, shoulder and lower pin regimes are found to be intact or separated, respectively, in the real experiment as well.

Figure 7. Development stages of the tools manufactured for verification. Base geometry without contouring, third and fifth design iterations with 1.8 mm and 2.6 mm structure width, respectively.

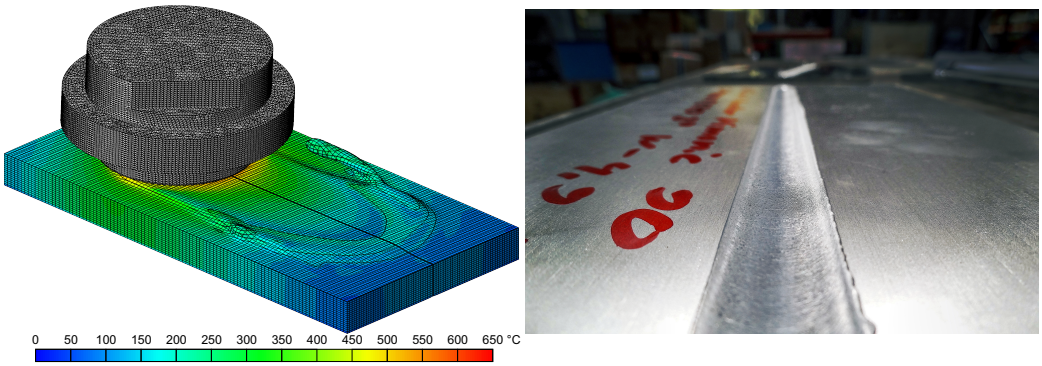

Figure 8. Outer appearance of weld carried out with the base geometry in simulation (**left**) and experiment (**right**).

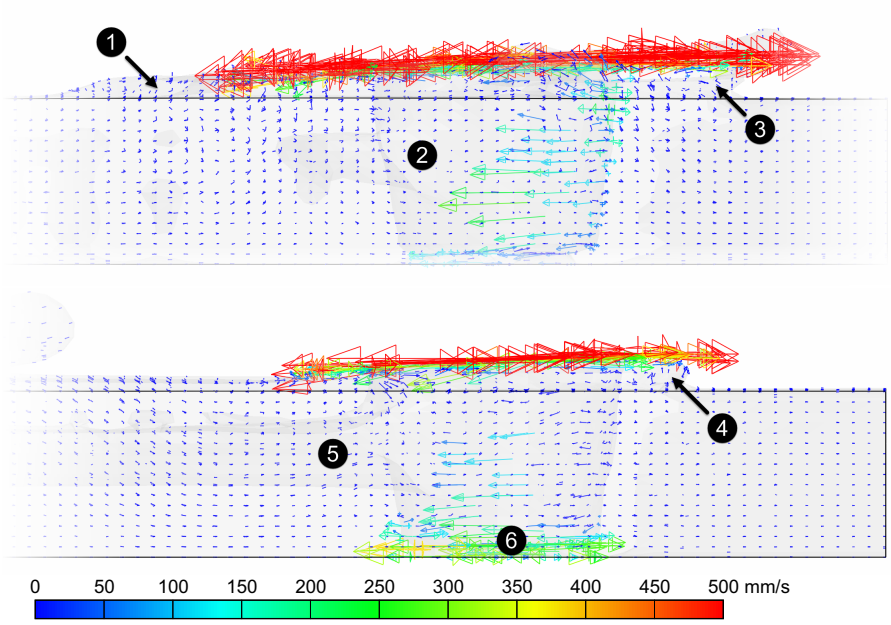

Figure 9. Semi-transparent section along the welding direction showing the local velocity distribution. At the top, shortly after the start of the traverse movement, at the bottom after reaching the process' steady state. Voids shaded, tool not shown.

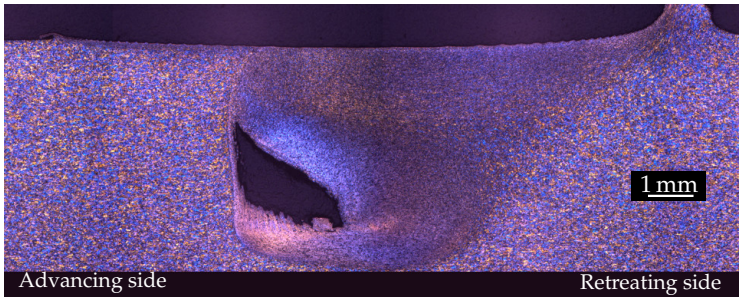

Figure 10. Barker-etched cross section of the real welding experimental corresponding to the steady state of Figure 9 with wormhole defect and burr formation on the right.

3.2. Results of Design Iterations and Comparison

In the previous section, the main causes of the defect formation for the base geometry were identified. These were an insufficient material flow within the joining zone, and the subsequent formation of a stagnation point, leading to a cavity. As mentioned above, the third design iteration of the tool was the first to exhibit no wormhole formation in sections during traversing in the simulation. Figure 11 shows a direct comparison of the base geometry to this third iteration with a structure width of 1.8 mm in top view. First of all, the location of the stagnation point can be clearly recognized for the base geometry (left) on the advancing side. In the area highlighted by the black ellipse, almost no material flow can be found at all. The velocity field of the third tool design iteration (right) clearly distinguishes from this. The three flutes induce an additional material flow with high velocities in the pin flow regime, exemplarily highlighted in the image by three black ellipses. With up to 450 mm/s, the velocities there reach about three to five times the values of the base geometry. This material flow resolves the former issue of the stagnation point very substantially. Furthermore, it becomes visible that the material flow structures homogenize the material flow overall. While very steep velocity gradients can be found between adjacent areas for the base geometry, such as velocities of 50 and 500 mm/s directly next to each other, the velocity field of the third design iteration is far

more homogeneous with significantly higher velocities in all flow regimes and far smoother transitions between them.

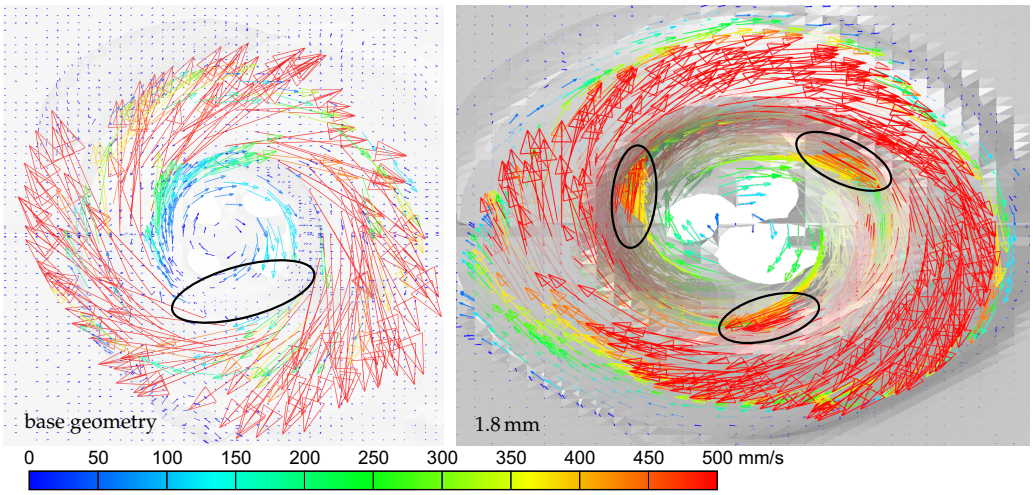

Figure 11. Velocity vectors for base geometry (**left**) and third design iteration with 1.8 mm structure width (**right**). Tools not shown. Ellipse left: stagnation point. Ellipses right: induced material flow by and within structure.

With further increasing the structure width, this tendency intensifies. Figure 12 shows the results of the fifth and final tool design iteration with a structure with of 2.6 mm. For a better perspective, the view is directed from the opposite side to the area of the former stagnation point. From the representation, the completely filled structure of the tool (labeled) and the high flow velocities induced by it can be recognized. In the area of the former worm hole, no signs of volumetric defect formation, such as indentations, can be found. The transitions between all material flow regimes are continuous and with smooth gradients. Thereby, the flow velocities in the upper area of the pin with 500 mm/s almost reach those of the shoulder regime.

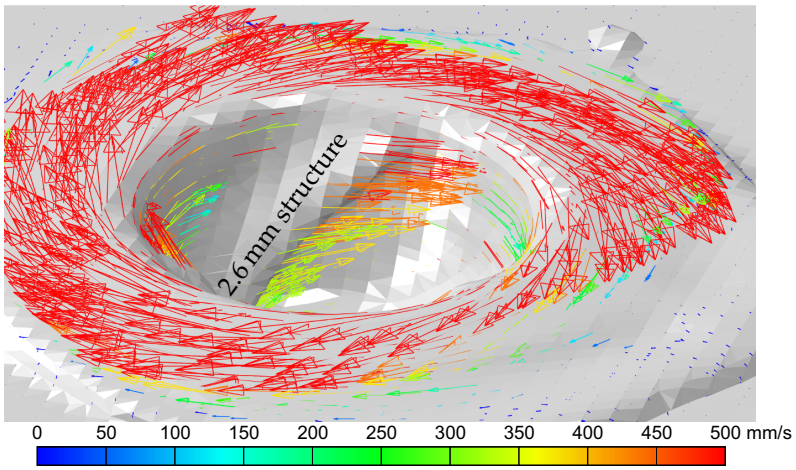

Figure 12. Material flow induced by the 2.6 mm wide structures of the fifth tool design iteration in the area of pin regime and former stagnation point. Tool not shown.

Figure 13 shows on the top the cross section of the welding experiment for the third design iteration (1.8 mm structure). The weld still shows a worm hole formation in the lower material flow regime of the pin on the advancing side. Defect location and also shape correspond very well to the defect caused by the base geometry. However, a significant reduction of the defect area from originally 3.4 mm² to less than 0.5 mm² is reached, reducing

the load-bearing cross section by about 14% (base geometry: 46%). Compared to the base geometry, a considerable improvement of the overall material flow in the weld can be recognized from the cross-section. Especially in the upper part of the pin regime towards the shoulder, the material flow is found more uniform and the material flow regimes consolidated. Same with the base geometry, the lower pin regime is well established. These findings correspond well to the results of the simulation. The material flow improvements are less pronounced in the center of the weld and close to the defect formation. As can be seen by the well visible white oxide layers (joint line remnants, highlighted by red arrow), the intermixing of the material is still not sufficient, and material flows are not fully merging in these areas. However, at the edges of the wormhole material flow structures can be observed (blue arrow). Those banded structures, cmp. Ref. [35], indicate an incipient material flow in those areas and that the volumetric defect is near closure. Taken together and as in the simulation, the defect formation of the third design iteration represents a transition case. In contrast to the simulation, the defect formation stabilized in the real welding experiment without closing again. Only near the starting point of the weld and so before reaching the steady state of the process, no wormhole occurred.

Figure 13 shows on the bottom the cross section of the welding experiment for the fifth design iteration with 2.6 mm structure. As predicted by the simulation, the weld no longer exhibits an inner volumetric defect. However, slight signs of a material flow disturbance can be detected at the former defect location (highlighted in the picture by a red circle). Compared to the third design iteration, weld and micro-structure are even more homogeneous. The material flow regimes are fully developed with smooth transitions between them, apart from a still slightly recognizable separation of the lower pin regime. No remaining oxide layers can be detected, and the material flow in the upper pin and shoulder regime further improved. In direct comparison with the other two welds, a further decrease in burr formation can be detected as well. This can be attributed to the fact that with increasing structure width, more and more material can be accommodated within the rotational volume of the tool, actively transported, and buffered. In the case of a structure width of 2.6 mm, already 15% of the pin's rotational volume is used for this purpose.

3.3. Further Consideration

Due to the highly coupled nature of the FSW process, the tool's structures not only influence directly the material flow, but through it, almost all other process phenomena. The most important one is the interaction of the material flow with the heat balance. Figure 14 shows a comparison of the temperature fields and gradients of the base geometry to the fifth design iteration during steady state. From the representation, it becomes clear that with the material flow a significant convective heat transfer within the joining zone takes place. By the structures, warmer material from the process' main heat source (shoulder) is transferred to deeper areas of the weld, homogenizing the temperature profile and simultaneously reducing the peak temperatures. While the base geometry shows temperature differences of more than 100 K between shoulder and center weld, the temperature differences of the fifth design iteration are less than 50 K. At the same time, both tool geometries show almost the same total heat input and so surface temperatures near the tool (highlighted by red circles). This more homogeneous heat distribution also reduces the flow resistance of the material and thus the overall resistance to the traverse movement of the tool. The base geometry resulted in a traverse force of about 1450 N in the real welding experiment and about 1350 N in the simulation. Contouring the pin with 2.6 mm structures led to a reduction of about 20.5% to 1150 N in the experiment and 18.5% to 1100 N in the simulation (means taken over 1.5 s, 150 and 60 values of steady state).

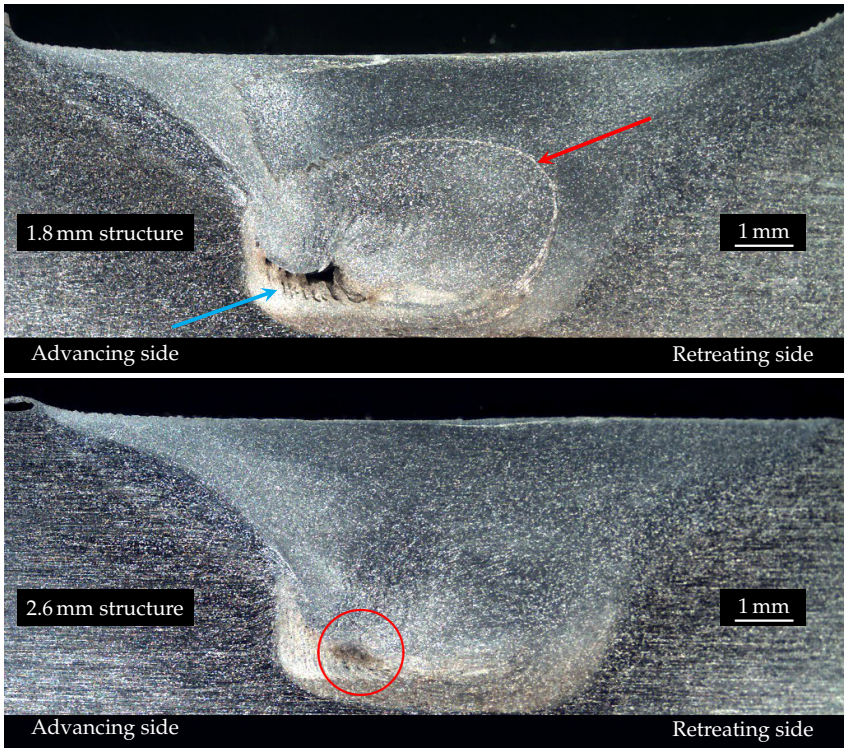

Figure 13. Etched cross sections of the welding tests carried out for validation with material flow representation at the (former) neuralgic stagnation point. 1.8 mm (**top**) and 2.6 mm (**bottom**) structure width.

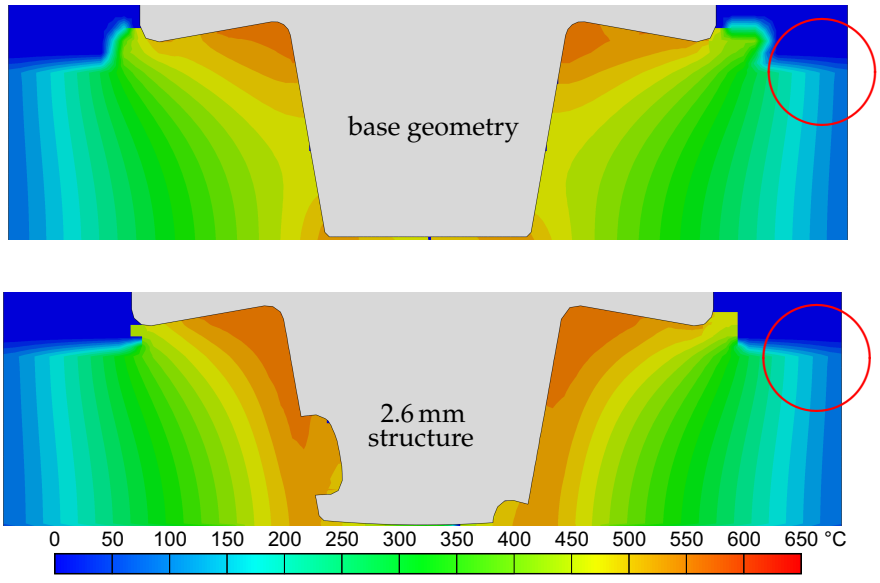

Figure 14. Comparison of temperature profiles and gradients in cross-section for base geometry (**top**) and fifth design iteration (**bottom**), e.g., with and without active material flow structures.

4. Discussion of Results

From the results, it becomes clear that the simulation framework is capable of representing all relevant process phenomena and aspects of FSW. Material flow and temperature fields, weld formation and welding defects can be predicted a priori and in high detail without calibrating the model on real welding experiments. This applies both to the outer appearance of the weld as well as the location, shape, and size of inner welding defects. Causes for defects can be identified and analyzed in detail. Compared to the real experi-

ment, the simulation showed a slight overestimation of the process impact in the case study, e.g., by predicting a closure of the void slightly to early. This may be attributed to the simplified modeling of material behavior via the Johnson–Cook model or the representation of boundary conditions. Since the error is small, simple differences in the setups of simulation and real experiment may be considered as cause as well. These may be tolerances in sheet thickness or plunging depth. Either way, the error appears to be acceptable in relation to the necessary efforts for modeling and data acquisition.

A very important aspect for numerical tool development is the precise simulation of highly detailed tool geometries and their effects. The case study shows that the numerical framework is capable of handling tool geometries and welding speeds similar to today's industrial and research applications. The effects of geometrical detailing on the process can be represented, predicted and assessed numerically with a high level of detail. In this context, the framework is capable of predicting the effects of active material flow structures on the local and the overall material flow in the joining zone. Important aspects, such as the accommodation of material within the rotational volume of the tool or the active convective heat transfer, are considered. A quantification of the effects of geometrical detailing on the highly coupled nature of the FSW process is possible. This concerns in particular the effect on the interaction of material flow and heat balance. Based on a common proxy, the development of the traverse force, the predictive power can be stated to be high.

Beyond these aspects, the very good suitability of (volumetric) welding defects for the evaluation of FSW process simulations becomes apparent from this study. These show a by far higher sensitivity to small process changes than most accessible FSW phenomena. Moreover, they are a result of and so a proxy for the whole and highly coupled FSW process itself, representing so all interactions of its phenomena. Furthermore, the importance to simulate the FSW process in one continuous simulation was underlined by the results. Welding defects may initiate during the plunging phase or the start of the traverse movement and propagate, evolve and persist into steady state.

5. Conclusions

In this study, a simulation framework able to predict the outcomes of the FSW process with a focus on numerical tool development was presented. The fully coupled thermomechanical three-dimensional simulation framework is based on Abaqus, using Noh's coupled Eulerian–Lagrangian formulation (CEL). For maximizing its general validity, the framework is based on fundamental physics and avoids fitting to welding experiments. For demonstrating the predictive power of the framework a numerical tool development case study was presented. Simulations were validated experimentally by real welding trials.

The framework is found to be capable of representing and predicting all relevant process phenomena and aspects of FSW. This allows the analysis of phenomena that are not directly accessible during the real welding process, e.g., due to restrictions stemming from FSW's working principle. The framework is capable of predicting forces, material flow and temperature fields, weld formation and welding defects a priori, in high detail and precisely. This applies both to the outer appearance of the weld as well as the location, shape, and size of inner welding defects. In the case study, defect sizes were predicted precisely with less than 5% difference to the experiment in relative terms. While the horizontal location of the wormhole defect was predicted well, its predicted vertical location differed from the validation experiment by about 20% of the sheet thickness. Traverse forces and their development with altering the size of the material flow structures were predicted with less than 10% relative error.

The case study showed that the numerical framework is capable of handling tool geometries with levels of detail and at welding speeds similar to today's industrial and research applications. Together with its predictive power, numerical tool development for FSW is directly possible. Necessary efforts for setting up the framework are comparable moderate and can use data which is already available. With the capabilities shown, next steps may include using the framework for systematically investigating tool wear and its

effects on welding process and results. In addition, the framework may be coupled with AI for finding completely new tool geometries or solving welding tasks automatically.

Funding: The simulation framework presented in this publication builds up on a method developed within project Ro 651/16-1 funded by the German Research Foundation (DFG).

Institutional Review Board Statement: Not applicable.

Informed Consent Statement: Not applicable.

Data Availability Statement: Further data such as videos is available from the author upon request.

Acknowledgments: In the very first place, the author wants to thank Rapid Technic AG, Switzerland, especially Heinz Weiss, for carrying out all welding experiments of this study and preparing most cross sections. Thanks are also due to Rudi Scheck from the MPA Stuttgart who prepared the barker etched cross section. Chris Kohler provided a unique numerical telephone counseling.

Conflicts of Interest: The author declares no conflict of interest.

References

1. Thomas, W.; Nicholas, E.; Needham, J.; Murch, M.; Temple-Smith, P.; Dawes, C. Improvements Relating to Friction Welding. U.K. Patent No. 9125978-8, 27 November 1992.
2. Arora, A.; De, A.; Debroy, T. Toward optimum friction stir welding tool shoulder diameter. *Scr. Mater.* **2011**, *64*, 9–12. [CrossRef]
3. Mehta, M.; Arora, A.; De, A.; Debroy, T. Tool Geometry for Friction Stir Welding—Optimum Shoulder Diameter. *Metall. Mater. Trans.* **2011**, *42*, 2716–2722. [CrossRef]
4. Sakamoto, Y. Tool Development by Numerical Simulation. In Proceedings of the 8th Symposium on Friction Stir Welding, Timmendorfer Strand, Germany, 18–20 May 2010.
5. Hossfeld, M.; Roos, E. A new approach to modelling friction stir welding using the CEL method. *Adv. Manuf. Eng. Technol.* **2013**, *2*, 179–190. [CrossRef]
6. Hamilton, R.; MacKenzie, D.; Li, H. Multi-physics simulation of friction stir welding process. *Eng. Comput.* **2010**, *27*, 967–985. [CrossRef]
7. Tutum, C.C.; Hattel, J.H. Numerical optimisation of friction stir welding: Review of future challenges. *Sci. Technol. Weld. Join.* **2011**, *16*, 318–324. [CrossRef]
8. Lorrain, O.; Serri, J.; Favier, V.; Zahrouni, H.; El Hadrouz, M. A contribution to a critical review of friction stir welding numerical simulation. *J. Mech. Mater. Struct.* **2009**, *4*, 351–369. [CrossRef]
9. Panzer, F.; Werz, M.; Weihe, S. Experimental investigation of the friction stir welding dynamics of 6000 series aluminum alloys. *Prod. Eng.* **2018**, *12*, 667–677. [CrossRef]
10. Liu, F.C.; Hovanski, Y.; Miles, M.P.; Sorensen, C.D.; Nelson, T.W. A review of friction stir welding of steels: Tool, material flow, microstructure, and properties. *J. Mater. Sci. Technol.* **2018**, *34*, 39–57. [CrossRef]
11. Chen, Z.W.; Cui, S. On the forming mechanism of banded structures in aluminium alloy friction stir welds. *Scr. Mater.* **2008**, *58*, 417–420. [CrossRef]
12. Zimmer, S.; Langlois, L.; Laye, J.; Bigot, R. Experimental investigation of the influence of the FSW plunge processing parameters on the maximum generated force and torque. *Int. J. Adv. Manuf. Technol.* **2010**, *47*, 201–215. [CrossRef]
13. Burford, D.; Britos, P.G.; Boldsaikhan, E.; Brown, J. Evaluation of friction stir weld process and properties for aerospace application: e-NDE for friction stir processes. In Proceedings of the 6th Annual Technical Review Meeting, FAA Joint Advanced Materials & Structures (JAMS), Washington, DC, USA, 19–20 May 2010.
14. Hattingh, D.G.; Blignault, C.; van Niekerk, T.I.; James, M.N. Characterization of the influences of FSW tool geometry on welding forces and weld tensile strength using an instrumented tool. *J. Mater. Process. Technol.* **2008**, *203*, 46–57. [CrossRef]
15. Hossfeld, M. Shoulderless Friction Stir Welding: A low-force solid state keyhole joining technique for deep welding of labile structures. *Prod. Eng.* **2022**, *16*, 389–399. [CrossRef]
16. Dawes, C.J.; Threadgill, P.L.; Spurgin, E.J.R.; Staines, D.G. *Development of the New Friction Stir Technique for Welding Aluminum Phase II*; TWI Member Report 5651/35/95; TWI: Cambridge, UK, 1995.
17. Thomas, W.M.; Staines, D.G.; Norris, I.M.; de Frias, R. Friction Stir Welding Tools and Developments. *Weld. World* **2003**, *47*, 10–17. [CrossRef]
18. Dawes, C.J.; Thomas, W.M. Development of improved tool designs for friction stir welding of aluminium. In Proceedings of the 1st International Conference on Friction Stir Welding, Thousand Oaks, CA, USA, 14–16 June 1999; pp. 2–6.
19. TWI Global. *Functions, Designs and Materials of Friction Stir Welding Tools*; TWI Global: Cambridge, UK, 2021.
20. Guerdoux, S.; Fourment, L. A 3D numerical simulation of different phases of friction stir welding. *Model. Simul. Mater. Sci. Eng.* **2009**, *17*, 075001. [CrossRef]
21. Assidi, M.; Fourment, L.; Guerdoux, S.; Nelson, T.W. Friction model for friction stir welding process simulation: Calibrations from welding experiments. *Int. J. Mach. Tools Manuf.* **2010**, *50*, 143–155. [CrossRef]

22. Hossfeld, M. A fully coupled thermomechanical 3D model for all phases of friction stir welding. In Proceedings of the 11th International Symposium on Friction Stir Welding, Cambridge, UK, 17–19 May 2016. [CrossRef]
23. Dialami, N.; Chiumenti, M.; Cervera, M.; Agelet de Saracibar, C. Challenges in thermo-mechanical analysis of friction stir welding processes. *Arch. Comput. Methods Eng.* **2017**, *24*, 189–225. [CrossRef]
24. Fraser, K.; Kiss, L.; St-Georges, L.; Drolet, D. Optimization of Friction Stir Weld Joint Quality Using a Meshfree Fully-Coupled Thermo-Mechanics Approach. *Metals* **2018**, *8*, 101. [CrossRef]
25. Bagheri, B.; Abbasi, M.; Abdolahzadeh, A.; Kokabi, A.H. Numerical analysis of cooling and joining speed effects on friction stir welding by smoothed particle hydrodynamics (SPH). *Arch. Appl. Mech.* **2020**, *90*, 2275–2296. [CrossRef]
26. Colegrove, P.A.; Shercliff, H.R. Experimental and numerical analysis of aluminium alloy 7075-T7351 friction stir welds. *Sci. Technol. Weld. Join.* **2003**, *8*, 360–368. [CrossRef]
27. Colegrove, P.A.; Shercliff, H.R. 3-Dimensional CFD modelling of flow round a threaded friction stir welding tool profile. *J. Mater. Process. Technol.* **2005**, *169*, 320–327. [CrossRef]
28. Liu, X.; Chen, G.; Ni, J.; Feng, Z. Computational Fluid Dynamics Modeling on Steady-State Friction Stir Welding of Aluminum Alloy 6061 to TRIP Steel. *J. Manuf. Sci. Eng.* **2017**, *139*, 051004. [CrossRef]
29. Hoßfeld, M. Experimentelle, Analytische und Numerische Untersuchungen des Rührreibschweißprozesses. Ph.D. Thesis, University of Stuttgart, Stuttgart, Germany, 2016. [CrossRef]
30. Arbegast, W.J. Application of Friction Stir Welding and Related Technologies. In *Friction Stir Welding and Processing*; Mishra, R.S., Mahoney, M.W., Eds.; ASM International: Materials Park, OH, USA, 2007; pp. 273–308.
31. Noh, W. CEL: A Time-Dependent, Two-Space-Dimensional, Coupled Eulerian-Lagrangian Code. *Methods Comput. Phys.* **1964**, *3*, 117–179.
32. Blau, P.J. *Friction Science and Technology: From Concepts to Applications*, 2nd ed.; CRC Press: Boca Raton, FL, USA, 2009.
33. Özışık, M.N. *Boundary Value Problems of Heat Conduction*; Dover Books on Engineering; Dover Publications: Newburyport, MA, USA, 2013.
34. Fletcher, L.S. *Conduction in Solids—Imperfect Metal-to-Metal Contacts: Thermal Contact Resistances, Section 502.5*; Heat Transfer and Fluid Mechanics Data Books; Genium Publishing Company: Schenectady, NY, USA, 1991.
35. Gratecap, F.; Girard, M.; Marya, S.; Racineux, G. Exploring material flow in friction stir welding: Tool eccentricity and formation of banded structures. *Int. J. Mater. Form.* **2012**, *5*, 99–107. [CrossRef]